

## Microscopic theory of optical gain in small semiconductor quantum dots

Y. Z. Hu, H. Gießen, and N. Peyghambarian

*Optical Sciences Center, University of Arizona, Tucson, Arizona 85721*

S. W. Koch

*Fachbereich Physik und Zentrum für Materialwissenschaften, Philipps-Universität Marburg, Renthof 5, 35112 Marburg, Germany*

(Received 10 July 1995; revised manuscript received 3 November 1995)

A microscopic theory is used to analyze optical gain in small semiconductor quantum dots. Based on a numerical matrix diagonalization method and subsequent solution of the optical Bloch equations, it is found that the quantum-dot gain is dominated by the stimulated transitions between biexciton and exciton states. The calculation shows that Coulomb interaction and valence-band mixing effects significantly influence the spectral and dynamic gain properties in strongly confined quantum dots.

### I. INTRODUCTION

In almost all commercial semiconductor lasers the emitted light is generated by the stimulated recombination of electron-hole pairs in the high-density carrier plasma. Under standard laser operation conditions the threshold carrier density is higher than the Mott density, so that bound electron-hole states are ionized because of the exchange interaction and screening of the attractive interband Coulomb potential. Therefore, it is usually a reasonable approximation to model the electron-hole plasma within the framework of the screened Hartree-Fock approximation. Such a treatment of the semiconductor gain medium allows us to explain many experimental findings and enables us to model laser and amplifier devices which are based on III-V semiconductor materials.<sup>1</sup>

On the other hand, since the late 1970s and early 1980s it has been well known that optical gain in wide-gap bulk semiconductors has significant excitonic and even biexcitonic contributions, at least under low-temperature operation conditions.<sup>2,3</sup> Indications for the influence of such strong electron-hole correlations have also been discussed recently in connection with laser action in II-VI quantum-well structures.<sup>4</sup> In these II-VI materials, the exciton binding energy is a few tens of meV, so that strong excitonic effects should be present even at laser threshold densities.

A satisfactory theoretical understanding of electron-hole correlation effects in bulk and quantum-confined semiconductor structures and their influence on the optical gain does not yet exist. This problem is not only interesting and challenging because of its many-body aspects but is also of significance for device development and optimization. As a step in the direction of understanding the influence of excitonic correlation effects on the gain in quantum-confined semiconductors, in this paper we study very small semiconductor structures, i.e., quantum dots (QD's). The strongly confined quantum dots are a model system for excitonic and biexcitonic gain contributions in their purest form since the quantum confinement leads to a complete absence of continuum states.

There is substantial interest in QD's as evidenced by the substantial number of theoretical and experimental studies

conducted to understand the linear and nonlinear optical properties of such systems.<sup>5</sup> These investigations revealed many unique properties of QD's compared with bulk semiconductors or semiconductor quantum wells. As an important insight one recognized that with increasing quantum confinement biexcitons play an increasingly important role in determining the optical nonlinearities.<sup>6,7</sup>

In recent experimental studies on small CdSe quantum dots, optical gain with a bandwidth of approximately 0.5 eV has been observed.<sup>8</sup> The detailed experimental study shows that the gain in the effectively zero-dimensional QD system differs significantly from that in bulk and quantum-well structures. For example, in QD's spectrally very broad optical gain can be realized from far below to well above the fundamental band gap, whereas in bulk and quantum-well structures plasma gain is possible only in the spectral region between the renormalized gap and the electron-hole quasi-chemical potential.

It is our goal in this paper to present and evaluate an idealized but realistic model for excitonic lasing in QD's. We demonstrate that the various biexciton-to-exciton transitions essentially determine the optical gain properties. To calculate the gain spectra, we first compute the exciton and biexciton states using a numerical matrix diagonalization method,<sup>7</sup> in which the Coulomb interaction, valence-band mixing,<sup>9</sup> and surface polarization effect<sup>10</sup> are included. The optical transition dipole moments are obtained from the computed exciton and biexciton wave functions. To study the optical gain dynamics and compute pump-probe spectra in the gain regime we solve the spatially Fourier-transformed multilevel optical Bloch equations. The results explain the broad gain spectra observed experimentally and reveal some interesting qualitative differences between the electron-hole plasma lasing mechanism and the gain mechanism from a strongly correlated excitonic system in a QD.

### II. THEORETICAL MODEL

The linear and nonlinear optical properties in the spectral region of the semiconductor band gap are determined by the electron-hole excitations. If one studies an intrinsic semiconductor system it is possible to describe the optical excitations

using electron-hole-pair states, i.e., excitons, biexcitons, and so on. This picture is especially useful in the case of small quantum dots. It is because, for dot sizes comparable to or smaller than the bulk exciton Bohr radius, the optical properties of QD's near the absorption edge are dominated by the exciton and biexciton states.<sup>5</sup> In this case, if the pump photon frequency is not high enough to excite electrons to the high-energy quantum confinement states, only exciton and biexciton states can be excited.

The electron-hole Hamiltonian can be written using the exciton and biexciton projection operators,<sup>5,7</sup>

$$H_0 = \sum_e \epsilon_x^e |e\rangle \langle e| + \sum_b \epsilon_{xx}^b |b\rangle \langle b|, \quad (1)$$

where  $|e\rangle$  and  $|b\rangle$  are the exciton and biexciton eigenstates. The corresponding energy eigenvalues  $\epsilon_x^e$  and  $\epsilon_{xx}^b$  are determined from the one- and two-pair Schrödinger equations

$$(H_e + H_h + V_{eh}) \sigma_x^e(s, j) \phi_x^e(\mathbf{r}_x, \mathbf{r}_h) = \epsilon_x^e \sigma_x^e(s, j) \phi_x^e(\mathbf{r}_e, \mathbf{r}_h), \quad (2)$$

and

$$\begin{aligned} & (H_{e_1} + H_{e_2} + H_{h_1} + H_{h_2} + V_{e_1, e_2} + V_{h_1, h_2} + V_{e_1, h_1} + V_{e_2, h_1} \\ & + V_{e_1, h_2} + V_{e_2, h_2}) \sigma_{xx}^b(s_1, s_2, j_1, j_2) \phi_{xx}^b(\mathbf{r}_{e_1}, \mathbf{r}_{e_2}, \mathbf{r}_{h_1}, \mathbf{r}_{h_2}) \\ & = \epsilon_{xx}^b \sigma_{xx}^b(s_1, s_2, j_1, j_2) \phi_{xx}^b(\mathbf{r}_{e_1}, \mathbf{r}_{e_2}, \mathbf{r}_{h_1}, \mathbf{r}_{h_2}), \end{aligned} \quad (3)$$

where  $\phi_x^e$  and  $\phi_{xx}^b$  are the spatial parts and  $\sigma_x^e$  and  $\sigma_{xx}^e$  are the corresponding spin parts of the exciton and biexciton wave functions, respectively. Here  $s = \pm \frac{1}{2}$  denotes the spin quantum number of the electrons and  $j$  is the spin of holes in the top valence bands, i.e.,  $j = \pm \frac{3}{2}, \pm \frac{1}{2}$ . Furthermore,  $H_e$  and  $H_h$  are the kinetic-energy Hamiltonians of electron and hole, and  $V$  is the Coulomb-interaction Hamiltonian.

In wide-gap semiconductors, the effective-mass approximation is usually used to describe the energy dispersion of the conduction band. In this approximation  $H_e$  is given by (we take  $\hbar=1$  throughout this paper)

$$H_e = -\frac{1}{2m_e} \nabla_e^2 + V_e(\mathbf{r}_e) + E_g, \quad (4)$$

where  $m_e$  is the electron effective mass,  $V_e$  is the quantum confinement potential for the conduction electron, and  $E_g$  is the band gap.

For the valence bands, however, the parabolic-band assumption is usually not sufficient because of the strong spin-orbit coupling existing in III-V and II-VI semiconductors. The Luttinger Hamiltonian<sup>9,11</sup> has been successfully applied to describe the valence-band structure near the  $\Gamma$  point in semiconductors with cubic symmetries and strong spin-orbit interaction. Within the framework of the  $\mathbf{k} \cdot \mathbf{p}$  theory, the quantum-confined hole states in the presence of spin-orbit interaction have been studied in QD's with infinite<sup>12</sup> or finite confinement potential.<sup>13</sup> A more sophisticated model for the hole quantum confinement levels has also been calculated, in which the spin-split-off bands are taken into account.<sup>14</sup> Using the so-called spherical approximation, where the Luttinger parameters  $\gamma_2 = \gamma_3$ , the Luttinger Hamiltonian can be reduced

into the form in which the Hamiltonian becomes irreducible under the full rotation group.<sup>11,12</sup>

$$H_h = \frac{\gamma_1}{2m_0} \left[ p_h^2 - \frac{\mu}{9} (p_h^{(2)} \cdot J^{(2)}) \right] + V_h(\mathbf{r}_h), \quad (5)$$

where  $m_0$  is the free-electron mass,  $\mu = 2\gamma_2/\gamma_1$ , and  $\gamma_1$  and  $\gamma_2 = \gamma_3$ , are the Luttinger parameters.  $V_h$  is the quantum confinement potential for the hole. In the Hamiltonian (5),  $p_h^{(2)}$  and  $J^{(2)}$  are the spherical tensors of rank 2 for the momentum operator  $p_h$  and the angular momentum operator  $J = \frac{3}{2}$ , respectively. Definitions of the spherical tensor operators and the dot product of two spherical tensors can be found in the Ref. 11. In order to keep the subsequent numerical calculations at a feasible level, in the present paper we restrict our analysis to cases where it is reasonable to assume an infinitely high quantum confinement potential and neglect the spin-split-off bands.

The Coulomb interaction  $V_{q_1, q_2}$  in Eqs. (2) and (3) includes two contributions: the direct Coulomb interaction and the surface polarization:<sup>10</sup>

$$\begin{aligned} V_{q_1 q_2}(\mathbf{r}_{q_1}, \mathbf{r}_{q_2}) &= \pm \frac{e^2}{\epsilon_2 |\mathbf{r}_{q_1} - \mathbf{r}_{q_2}|} + Q_1(\mathbf{r}_{q_1}) + Q_1(\mathbf{r}_{q_2}) \\ &\quad \pm Q_2(\mathbf{r}_{q_1}, \mathbf{r}_{q_2}). \end{aligned} \quad (6)$$

The surface polarization, which is caused by the induced charges on the dielectric interface, is described by the Hamiltonian<sup>10</sup>

$$Q_1(\mathbf{r}) = \frac{e^2}{2R} \sum_{l=0}^{\infty} \alpha_l \left[ \frac{r}{R} \right]^{2l},$$

$$Q_2(\mathbf{r}_1, \mathbf{r}_2) = \frac{e^2}{R} \sum_{l=0}^{\infty} \alpha_l \left[ \frac{r_1 r_2}{R} \right]^l P_l[\cos(\theta)],$$

where

$$\alpha_l = \frac{(\epsilon - 1)(l + 1)}{\epsilon_2(l\epsilon + l + 1)}.$$

In these equations,  $P_l$  is the  $l$ th-order Legendre polynomial, and  $\epsilon = \epsilon_2/\epsilon_1$  with  $\epsilon_2$  ( $\epsilon_1$ ) the dielectric constant inside (outside) the quantum dot.  $\theta$  is the angle between the position vectors  $\mathbf{r}_1$  and  $\mathbf{r}_2$ .  $R$  is the radius of the microcrystal. The + (−) sign in Eq. (6) is for the equal (opposite) charge sign of the two particles.

In our calculations we first obtain the exciton and biexciton eigenstates of Eqs. (2) and (3) using the numerical matrix diagonalization method, which is discussed in the Appendix. A summary of basic excitonic properties in quantum dots is given in the Appendix. Using the exciton and biexciton energy levels and wave functions, we then calculate the optical properties of QD's by solving the multilevel optical Bloch equations.

### III. MULTILEVEL OPTICAL BLOCH EQUATIONS

For low-excitation conditions the nonlinear optical properties can be approximated using only the lowest-order nonlinear susceptibility  $\chi^{(3)}$ .<sup>7</sup> The continuous-wave approxima-

tion often makes it possible to obtain analytical expressions of  $\chi^{(3)}$ . Thus, for given exciton and biexciton energies and dipole moments, one can calculate the optical nonlinearities such as one-beam saturation, two-photon absorption, four-wave mixing, and pump-probe spectra. However, for highly excited systems such as the QD with gain the knowledge of higher-order nonlinearities is necessary. Therefore, in order to calculate optical response functions in the high-excitation regime, we need to numerically solve the multilevel optical Bloch equations.

In the presence of an external laser field  $\mathbf{E}$ , the Hamiltonian becomes

$$H = H_0 - \sum_e \mu_{eo} |e\rangle \langle o| - \sum_{eb} \mu_{be} |b\rangle \langle e| - \text{c.c.} \quad (7)$$

In Eq. (7)  $\mu_{ij} = \mathbf{d}_{ij} \cdot \mathbf{E}$ , where  $\mathbf{d}_{ij}$  is the dipole moment between the states  $|i\rangle$  and  $|j\rangle$ . This dipole moment is proportional to the interband dipole moment  $p_{cv}$  and the overlap of the electron and hole wave functions.<sup>7</sup> The density matrix

$$\begin{aligned} \rho = & \rho_{oo} |o\rangle \langle o| + \sum_{ee'} \rho_{ee'} |e\rangle \langle e'| + \sum_{bb'} \rho_{bb'} |b\rangle \langle b'| \\ & + \sum_e (\rho_{eo} |e\rangle \langle o| + \text{H.c.}) + \sum_{be} (\rho_{be} |b\rangle \langle e| + \text{H.c.}) \\ & + \sum_b (\rho_{bo} |b\rangle \langle o| + \text{H.c.}) \end{aligned} \quad (8)$$

is then determined by Liouville's equation

$$i \frac{d\rho}{dt} = [H, \rho]. \quad (9)$$

Inserting Eq. (8) into Eq. (9), one obtains the equations of motion for the density-matrix expansion coefficients,

$$\begin{aligned} i \frac{d\rho_{eo}}{dt} &= \epsilon_x^e \rho_{eo} + \sum_{e'} \mu_{e'o} \rho_{ee'} - \sum_b \mu_{eb} \rho_{bo} - \mu_{eo} \rho_{oo}, \\ i \frac{d\rho_{be}}{dt} &= (\epsilon_{xx}^b - \epsilon_x^e) \rho_{be} - \sum_{e'} \mu_{be'} \rho_{e'e} + \sum_{b'} \mu_{b'e} \rho_{bb'} \\ &+ \mu_{oe} \rho_{bo}, \\ i \frac{d\rho_{ee'}}{dt} &= (\epsilon_x^e - \epsilon_x^{e'}) \rho_{ee'} + \mu_{oe'} \rho_{eo} - \mu_{eo} \rho_{oe'} \\ &- \sum_b (\mu_{eb} \rho_{be'} - \mu_{be'} \rho_{eb}), \\ i \frac{d\rho_{bb'}}{dt} &= (\epsilon_{xx}^b - \epsilon_{xx}^{b'}) \rho_{bb'} + \sum_e (\mu_{eb'} \rho_{be} - \mu_{be} \rho_{eb'}), \\ i \frac{d\rho_{bo}}{dt} &= \epsilon_{xx}^b \rho_{bo} - \sum_e (\mu_{be} \rho_{eo} - \mu_{eo} \rho_{be}), \\ \rho_{oo} &= 1 - \sum_e \rho_{ee} - \sum_b \rho_{bb}. \end{aligned} \quad (10)$$

Using the solutions of these equations, the optical polarization is calculated as

$$\langle \mathbf{P}(t) \rangle = \sum_e \mathbf{d}_{oe} \rho_{eo}(t) + \sum_{eb} \mathbf{d}_{eb} \rho_{be}(t). \quad (11)$$

The optical properties of QD's, such as absorption/gain and refractive index, are then determined by Eqs. (10) and (11). The task is to solve Eqs. (2) and (3) to obtain the exciton and biexciton energies  $\epsilon_x^e$  and  $\epsilon_{xx}^b$  and optical dipole moments  $d_{eo}$  and  $d_{be}$  and then to solve Eqs. (10) and (11) to obtain the optical gain spectra.

#### IV. OPTICAL GAIN IN QUANTUM DOTS

In the simplest theoretical description of quantum dots, in which both Coulomb-interaction and valence-band-mixing effects are neglected, only the transitions between the quantum-confined electron and hole levels with identical envelope quantum numbers are dipole allowed. However, this simple selection rule is substantially modified by the inclusion of the valence-band mixing and electron-hole Coulomb interaction. As shown in previous theoretical studies, the strong coupling of the hole  $s$  and  $d$  wave functions leads to additional, dipole-allowed transitions near the lowest electron-hole-pair excitation.<sup>12</sup> The Coulomb interaction also causes a series of additional, otherwise dipole-forbidden transitions between exciton and biexciton states.<sup>7</sup>

Using the exciton and biexciton wave functions obtained from the numerical matrix diagonalization, we calculate the optical transition dipole moments between the exciton and ground states and between the exciton and biexciton states, respectively. In Fig. 1(a), we show a simplified sketch of the relevant exciton and biexciton levels near the absorption edge. As shown by Xia,<sup>12</sup> the transition between the ground state and the state  $|1s, 1d_{3/2}\rangle$  is dipole allowed because of the valence-band mixing. Here we denote the electron-hole-pair states using only the quantum numbers of the most strongly contributing unperturbed basis state. For example, in the exciton ground state, the unperturbed basis is  $|1s, 1s_{3/2}\rangle$  and the real exciton wave function has its dominant contribution from the state  $|1s, 1s_{3/2}\rangle$  with significant mixing of  $|1s, 1d_{3/2}\rangle$ ,  $|1s, 2s_{3/2}\rangle$ ,  $|1p, 1p_{3/2}\rangle$ , etc.

The selection rules are somewhat more complicated for the exciton-to-biexciton transitions. A schematic illustration is shown in Fig. 1(a) where the original dipole-allowed states are indicated by the solid arrows, whereas the additional transitions induced by the valence-band mixing are indicated by the dashed arrows. Those transitions which become dipole allowed as a consequence of the Coulomb interaction are illustrated by the dotted arrows. The upward arrows represent the optical pump processes that create the population inversion in the QD system. The downward arrows in Fig. 1(a) indicate those transitions between exciton and biexciton states and between the exciton and the vacuum state which contribute to the stimulated emission process. Although these transitions can be understood already from symmetry arguments, the relative strengths of the dipole moments can be obtained only from numerical calculations.

In Fig. 1(b), we plot the computed dipole moments and the corresponding resonance frequencies. To calculate the dipole moments, we choose the size of the quantum dot  $R =$

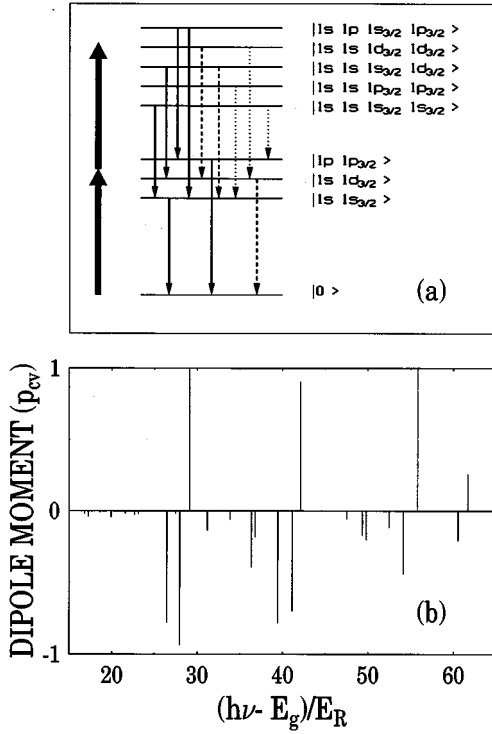


FIG. 1. (a) Exciton and biexciton energy levels of a quantum dot.  $|0\rangle$  is the ground state.  $|1s, 1s_{3/2}\rangle$  is the exciton ground state and  $1s$  and  $1s_{3/2}$  denote the orbital angular momentum quantum numbers of electron ( $1s$ ) and hole ( $1s_{3/2}$ ), respectively.  $|1s, 1s, 1s_{3/2}, 1s_{3/2}\rangle$  is the lowest biexciton state. The dark upward arrows indicate the optical pump process and solid downward arrows indicate the stimulated emissions that are dipole allowed without the Coulomb-interaction or valence-band-mixing effect. The dashed arrows show the stimulated recombination induced by the valence-band-mixing effect and the dotted arrows show the stimulated recombination induced by the Coulomb interaction. (b) Computed dipole moments between the exciton states and ground state (upper half) and between the biexciton states and exciton states (lower half). The material parameters are  $R=0.5a_B$ ,  $m_e=0.2m_0$ ,  $\gamma_1=5.0$ ,  $\mu=0.75$ ,  $\varepsilon_2=10$ , and  $\varepsilon_1=1$ .

$\frac{1}{2}a_B$ ,  $m_e=0.2m_0$ ,  $\gamma_1=5.0$ ,  $\mu=0.75$ , and  $\varepsilon_2=10$  and  $\varepsilon_1=1$ . The exciton units used in this section, such as the effective Bohr radius  $a_B$  and effective Rydberg energy  $E_R$  are defined explicitly in the Appendix. With the material parameters used in this calculation, we find  $a_B=53 \text{ \AA}$  and  $E_R=13.6 \text{ meV}$ .

Some qualitative conclusions regarding the gain spectrum can be drawn from Fig. 1. (i) If the biexciton states are initially populated, optical gain can be realized by stimulated transitions between the biexciton and the exciton states. (ii) Optical gain in a spectrally broad region is possible in such a system, e.g., it can be seen from Fig. 1(b) that stimulated emission can occur far below the absorption edge. This redshifted stimulated emission, in comparison to the absorption, can be explained as follows: as a consequence of the positive biexciton binding energy, the strong stimulated emission from the ground-state biexciton  $|1s, 1s, 1s_{3/2}, 1s_{3/2}\rangle$  to the ground-state exciton  $|1s, 1s_{3/2}\rangle$  has a lower energy than the energetically lowest linear absorption process.

Furthermore, there are some comparatively weaker emission contributions that lead to gain energetically below the

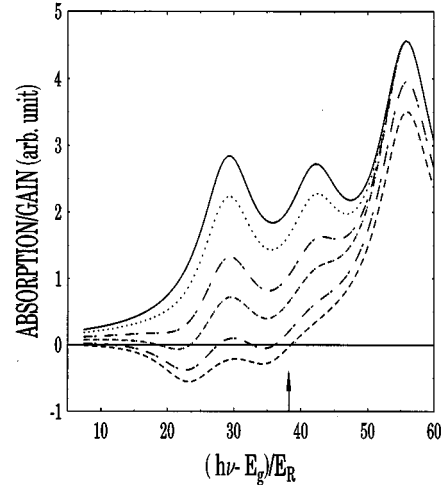


FIG. 2. Computed linear absorption (solid) and bleached absorption/gain spectra (dashed) with various biexciton or exciton populations. The material parameters are the same as in Fig. 1(b). The homogeneous dephasing time is chosen as 10 fs. From top to bottom, dashed curves correspond to increasing biexciton or exciton population. The arrow shows one-half of the maximum biexciton energy that was populated in the calculation.

transition between the ground-state biexciton and ground-state exciton. These contributions result from transitions between the biexciton states and the excited exciton states. For instance, the stimulated emission between  $|1s, 1s, 1s_{3/2}, 1s_{3/2}\rangle$  and  $|1p, 1p_{3/2}\rangle$  has a lower energy than the lowest exciton absorption resonance.

There is some superficial similarity between the redshift of gain in quantum dots and the band-gap-renormalization phenomenon in bulk or quantum-well samples. Clearly, the redshifts of optical gain in quantum dots and in extended semiconductor structures are both caused by Coulomb correlations. However, there is some basic difference, as one can see from the simple argument that in quantum dots the redshifted gain mostly occurs because of the transitions between the biexciton ground state and excited exciton states. In the biexciton ground state, both electrons (holes) have antiparallel spin and there is no exchange interaction. However, it is the exchange interaction that makes a significant contribution to the band-gap renormalization in bulk or quantum wells.

To quantify the above arguments, we performed a numerical study of the gain properties in quantum dots by solving the multilevel optical Bloch equations, Eqs. (10). The equations are spatially Fourier transformed according to the pump and probe propagation directions. To extract only the leading contributions the pump field is kept up to the second order whereas the probe field is kept only in the first order. The numerical integration is performed using a fourth-order Runge-Kutta method.

In Fig. 2, we plot the calculated linear absorption spectrum (solid curve) for the same parameters used in Fig. 1(b). The homogeneous dephasing time is chosen as 10 fs. The first two absorption resonances correspond to the transitions between the ground state and  $|1s, 1s_{3/2}\rangle$  and  $|1s, 1d_{3/2}\rangle$ .

To simulate the saturation and gain effects in optically pumped quantum-dot systems, we also calculate the absorption/gain spectra for various initial exciton and biex-

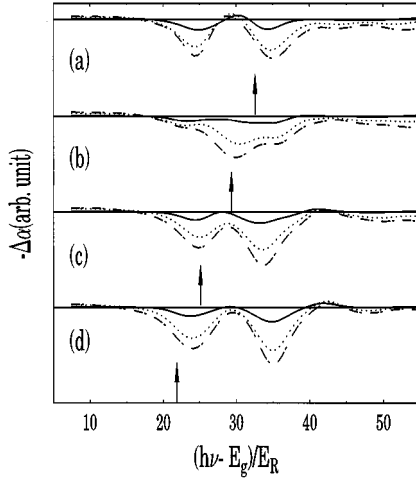


FIG. 3. Computed differential transmission spectra corresponding to the lowest gain curve in Fig. 2. The time delay between the pump and probe pulse is 0. The duration of the pump pulse is 50 fs. The arrows indicate the center pump frequencies.

citon distributions. We assume that the incoherent relaxation processes cause a uniform distribution of the biexciton (exciton) population over those states which are energetically below the pump photon energy.

The series of dashed curves in Fig. 2 shows the results obtained for different initial biexciton populations. Since we only account for exciton and biexciton contributions in the multilevel optical Bloch equations, Eqs. (10), the absorption is completely bleached if the biexciton population in a dot reaches unity. However, in reality, the transitions between the biexciton states and triexciton states contribute to an absorption background on the high-energy side. To include this absorption background in the gain spectrum, we also calculate the linear absorption solely due to the transitions from the ground state to the exciton states energetically higher than the exciton state  $|1p, 1p_{3/2}\rangle$  and assume that these transitions are not strongly influenced by the presence of the biexciton states on the low-energy side of the spectrum. We want to emphasize at this point that this partially phenomenological treatment of the absorption background has no qualitative impact on the gain region in Fig. 2 or on the subsequent discussion of pump-probe spectra.

Assuming a situation where optical gain exists and exciting the system with an additional strong pulse (sometimes called a pump pulse), we compute the probe spectra in the gain regime. Experiments of this kind have been performed for bulk semiconductors, as reported, e.g., in Ref. 15. For our quantum-dot model we show in Fig. 3 the resulting differential transmission spectra (DTS) for various pump frequencies and pump pulse intensities. The parameters are the same as those used to calculate the lowest gain spectrum in Fig. 2. Temporal overlap of the maxima of the strong pulse and the probe pulse is assumed. The arrows in the different parts of Fig. 3 indicate the respective energies of the strong pulse.

Our results show that the entire gain region is simultaneously depleted by the strong pulse, which is amplified through stimulated photon emission. Furthermore, there appears stronger bleaching on the high-energy side of the gain spectrum when the strong pulse is tuned to the low-energy

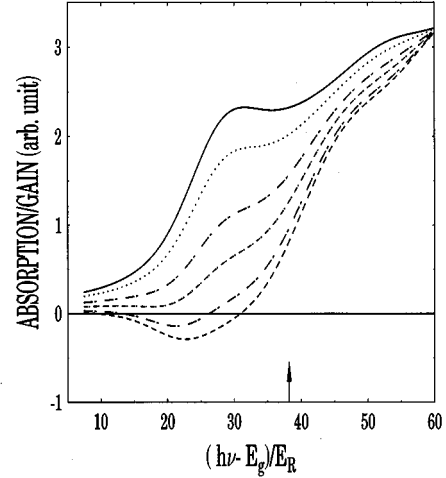


FIG. 4. Computed linear absorption (solid) and bleached absorption/gain spectra (dashed) for dots with a Gaussian size distribution. The field and material parameters are the same as in Fig. 2. The width of the Gaussian size distribution is  $0.1R$ . From top to bottom, dashed curves correspond to increasing biexciton or exciton population.

side of the gain [Figs. 3(d) and 3(c)]. In contrast to bulk or quantum-well systems where carrier reequilibration has to occur after the frequency-selective carrier removal through the strong pulse, the gain depletion at all the frequencies involved in the quantum-dot gain occurs on a very fast time scale determined by the biexciton-to-exciton transition time, independent of the pulse duration and of the pump-probe delay. The reason for this behavior is the fact that the low-energy pump photon bleaches not only the transition between  $|1s, 1s, 1s_{3/2}, 1s_{3/2}\rangle$  and  $|1s, 1s_{3/2}\rangle$  but simultaneously also the transition between  $|1s, 1s, 1s_{3/2}, 1d_{3/2}\rangle$  and  $|1s, 1d_{3/2}\rangle$  [see Fig. 1(a)]. This second transition is bleached even more strongly than the first one if the pump photon is tuned below the first transitions because the binding energy of the biexciton state  $|1s, 1s, 1s_{3/2}, 1d_{3/2}\rangle$  is larger than that of  $|1s, 1s, 1s_{3/2}, 1s_{3/2}\rangle$ . Since the stimulated emission occurs from the biexciton state  $|1s, 1s, 1s_{3/2}, 1d_{3/2}\rangle$  one has simultaneous phase-space blocking of the transition between  $|1s, 1s, 1s_{3/2}, 1d_{3/2}\rangle$  and  $|1s, 1s_{3/2}\rangle$ , which is the major contributor to the gain on the high-energy side of the spectrum.

To study the influence of the size distribution of quantum dots, which often plays a major role in realistic systems, we extend our analysis to include this inhomogeneous broadening effect. Figures 4 and 5 present the results corresponding to Figs. 2 and 3, where we used the same material parameters as in Fig. 2 but additionally assumed a Gaussian size distribution with a standard deviation of 10%. The calculated linear absorption and gain are shown in Fig. 4. In comparison to Fig. 2, we see that both absorption and gain spectra are significantly broadened, as expected for an inhomogeneous system.

Figure 5 shows the calculated DTS in the inhomogeneously broadened quantum-dot sample. The same pumping parameters as in the strongest (lowest) gain spectrum in Fig. 3 have been used. As in Fig. 3, when the pump frequency is tuned to the low-energy side of the gain spectrum, we find the double-dip feature, which is even enhanced by the inho-

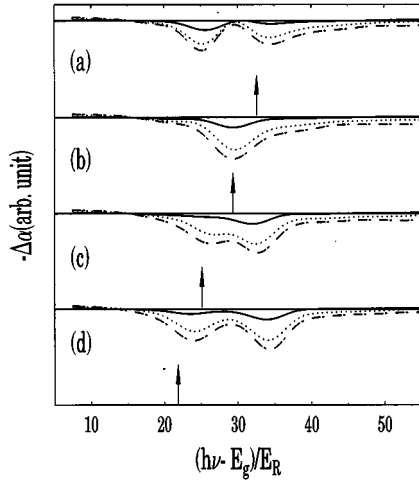


FIG. 5. Computed differential transmission spectra corresponding to the lowest gain curve in Fig. 4. The field and material parameters are the same as in Fig. 4. The time delay between the pump and probe pulse is 0. The duration of the pump pulse is 50 fs. The arrows indicate the center pump frequencies.

mogeneous broadening. Characteristically for inhomogeneously broadened systems, we clearly see the hole-burning effect in Figs. 5(b) and 5(c), where the pump is tuned into the gain region but below the absorption edge.

So far, our qualitative analysis and numerical calculations clearly show the importance of the Coulomb interaction on the gain properties in small quantum dots. However, our numerical study also reveals that the commonly used parabolic-band approximation, in which the valence-band-mixing effect is ignored, is a dangerous approximation. To show the importance of the band mixing, we recalculated Figs. 4 and 5 using the parabolic-band approximation and the same material and pump parameters as before. The resulting absorption/gain spectra are shown in Fig. 6 and the DTS corresponding to the strongest gain is plotted in Fig. 7. In

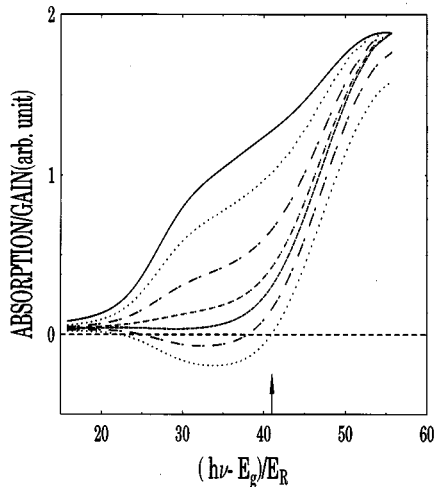


FIG. 6. Computed linear absorption (solid) and bleached absorption/gain spectra (dashed) for dots with a Gaussian size distribution. The field and material parameters are the same as in Fig. 4 except  $\mu=0$ .

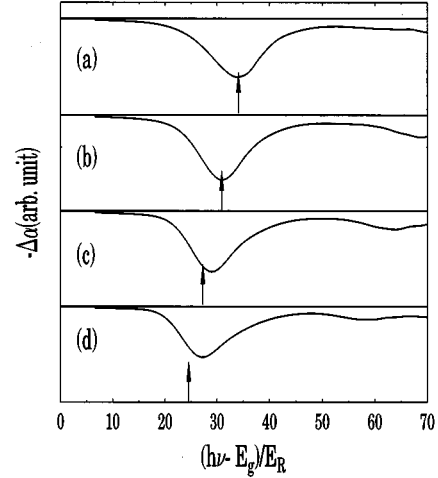


FIG. 7. Computed differential transmission spectra corresponding to the lowest gain curve in Fig. 5. The field and material parameters are the same as in Fig. 4 except  $\mu=0$ .

contrast to the rich structures seen in Fig. 5, Fig. 7 only shows the simple hole-burning effect which naturally occurs as a consequence of the inhomogeneous broadening. Thus, although one might succeed in fitting absorption spectra using the parabolic-band approximation, the complicated nature of experimental pump-probe spectra<sup>8</sup> cannot be understood without taking the valence-band nonparabolicity into account.

## V. EXPERIMENTAL RESULTS

In order to verify the model, femtosecond pump-probe experiments have been performed. A 115-fs pump pulse at 560 nm with 7 nm full width at half maximum (FWHM) excited a CdSe quantum-dot sample, which was held at 10 K. The average radius of the dots was about 25 Å (size distribution 15%), which is about half the exciton Bohr radius of CdSe. The dots were embedded in a borosilicate glass matrix which was 200  $\mu\text{m}$  thick. After 5 ps, a white-light femtosecond pulse probed the absorption. The change in the absorption ( $-\Delta\alpha L$ ) is plotted in Fig. 8 for various excitation intensities. At low pump intensities, gain develops from the low-energy side of the spectrum, extending at the highest pump intensity from below 660 to 560 nm. At the highest pump intensities, the magnitude of the low-energy gain exceeds the magnitude of the linear  $\alpha L$  spectrum. The experimental data agree very well with the theoretical calculations. The inset to Fig. 8 shows the same experimental data as Fig. 8, except that the probe-beam absorption  $\alpha L$  is plotted instead of the  $-\Delta\alpha L$  signal. In the case of maximum pump intensity  $I_0$ , the gain has a maximum value of  $\sim\alpha L=0.28$  (22% of linear absorption). Gain can be observed for the first time in the spectra at a pump intensity of  $I_0/32$ . From the spectra it can be clearly seen that the maximum gain occurs at different spectral positions compared to the peaks in the linear absorption, therefore demonstrating that the gain does not arise only from the inverted one-pair states.

## VI. SUMMARY

In this paper, we present a microscopic model calculation of the excitonic and biexcitonic lasing mechanism in small

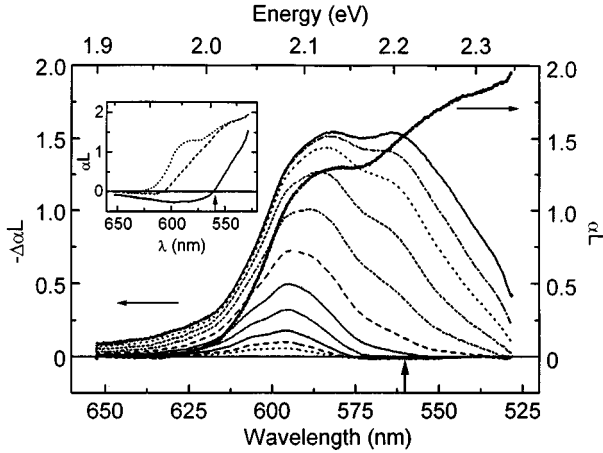


FIG. 8. Experimental differential absorption at  $t=5$  ps for increasing intensities  $I_0, I_0/2, I_0/4, I_0/8$ , etc. ( $I_0=25$  mJ/cm<sup>2</sup>,  $T=10$  K, pump wavelength=560 nm.) The inset shows the linear absorption (solid) and the absorption spectra at  $I_0$  (dotted) and  $I_0/32$  (dashed).

semiconductor quantum dots. Our calculations attribute the optical gain to the stimulated emission involving transitions between the quantum-confined biexciton states and the exciton states. We calculate the optical response of quantum dots by numerically solving the multilevel optical Bloch equations. The exciton and biexciton wave functions and eigenenergies are determined using the numerical diagonalization method, in which we need only bulk material parameters such as the electron effective mass, the Luttinger parameters, and dielectric constants of the semiconductor and host material. The numerical matrix diagonalization allows us to include many important interactions, such as Coulomb and valence-band-mixing effects.

The numerical results qualitatively explain the recently observed optical gain spectra in CdS quantum dots.<sup>8</sup> We show that spectrally broad optical gain in small quantum dots occurs as a consequence of the strong Coulomb correlations. The biexcitonic processes make it possible to have gain spectrally below the absorption edge and above the pump photon energy. Furthermore, our results clearly demonstrate that Coulomb-interaction and valence-band-mixing effects have characteristic signatures in the gain spectra.

#### ACKNOWLEDGMENTS

We thank M. Lindberg and U. Woggon for helpful and stimulating discussions. We acknowledge financial support from NSF, ARO, AFOSR, and the Deutsche Forschungsgemeinschaft, partially through the Sonderforschungsbereich 383.

#### APPENDIX: EXCITON AND BIEXCITON STATES

Generally, the direct numerical solution of the differential equations (2) and (3) is impractical if not completely impossible for exciton or biexciton problems because of the complicated interactions and boundary conditions. However, in

small quantum dots, where the dot radii  $R$  are comparable to or smaller than the exciton Bohr radius in the bulk sample, the Coulomb interaction can be treated perturbatively with respect to the quantum confinement energy. This fact allows us to use the so-called numerical matrix diagonalization or configuration-interaction method, to obtain numerically accurate exciton and biexciton energies as well as the corresponding wave functions. The details of the numerical matrix diagonalization method are discussed in Ref. 7 for the parabolic-band model. The underlying principle of this method is that the kinetic-energy eigenstates form a complete basis set in the Hilbert space which can be used to expand the exact exciton or biexciton wave functions. In practice, it is often possible to approximate the infinite Hilbert space by a finite linear space, in which the finite Hamiltonian matrices can be diagonalized numerically. The procedure of increasing the number of linearly independent basis states leads to a check of the desired numerical accuracy. To ensure numerical convergence, it becomes vital to choose appropriate basis functions. One of the techniques that made our earlier computations possible<sup>7</sup> is to make use of the conservation of the total angular momentum of the quantum-dot exciton or biexciton states in the presence of Coulomb interaction.

Unfortunately, if one goes beyond the parabolic-band approximation the orbital angular momentum of the exciton is no longer a good quantum number because of the  $\mathbf{k} \cdot \mathbf{p}$  interactions. However, as long as we can neglect the warping terms in the Luttinger Hamiltonian and apply the Hamiltonian (5), we can show that the total angular momentum  $\mathbf{F}_x = \mathbf{S}_e + \mathbf{J}_h + \mathbf{L}_e + \mathbf{L}_h$  is conserved. Here, we denote the intrinsic angular momentum of the conduction (valence) band by  $\mathbf{s}_e$  ( $\mathbf{j}_h$ ), and the corresponding envelope angular momentum by  $\mathbf{L}_e$  ( $\mathbf{L}_h$ ). Thus we have  $s_e = \frac{1}{2}$ ,  $j_h = \frac{3}{2}$ , and  $L_e, L_h = 0, 1, \dots$ . We choose the eigenstates of the total angular momentum operator  $\mathbf{F}$  as our basis states.

In general, we can express the exciton basis states as

$$\begin{aligned} & |n_e, l_e, n_h, l_h; L, J; F_x, F_{xz}\rangle_x \\ &= \sum \langle L, J; M, J_z | F_x, F_{xz} \rangle \langle l_e, l_h; m_e, m_h | L, M \rangle \\ & \quad \times \langle \frac{1}{2}, \frac{3}{2}; s_z, j_z | J, J_z \rangle |n_e, l_e, m_e; \frac{1}{2}, s_z\rangle |n_h, l_h, m_h; \frac{3}{2}, j_z\rangle. \end{aligned} \quad (\text{A1})$$

Here, the terms  $\langle l_1, l_2; m_1, m_2 | l, m \rangle$  are the Clebsch-Gordan coefficients in the Condon-Shortly notation.<sup>16</sup> We use the orbital quantum numbers  $n, l$ , and  $m$  and spin quantum numbers to denote the single-particle state  $|n, l, m; \frac{3}{2}, j_z\rangle$  for the hole and  $|n, l, m; \frac{1}{2}, s_z\rangle$  for the electron. If the quantum confinement potential is assumed to be infinitely deep, the orbital wave function can be explicitly expressed in terms of spherical Bessel functions and spherical harmonics.<sup>5</sup>

In a similar manner, we choose the eigenstates of the biexciton total angular momentum operator, which is defined as  $\mathbf{F}_{xx} = \mathbf{F}_{e_1} + \mathbf{F}_{e_2} + \mathbf{F}_{h_1} + \mathbf{F}_{h_2}$ , as the basis functions for the expansion of the biexciton wave functions. In order to take into account the proper antisymmetrization for identical fermions, we follow the two-band calculation<sup>7</sup> and construct the basis states as

$$\begin{aligned}
& |n_{e_1}, l_{e_1}, n_{e_2}, l_{e_2}, n_{h_1}, l_{h_1}, n_{h_2}, l_{h_2}; L_e, L_h, S_e, J_h, F_e, F_h; F_{xx}, F_{xxz}\rangle_{xx} \\
& = \sum \langle F_e, F_h; F_{ez}, F_{hz} | F_{xx}, F_{xxz} \rangle |n_{e_1}, l_{e_1}, n_{e_2}, l_{e_2}; L_e, S_e; F_e, F_{ez}\rangle_e |n_{h_1}, l_{h_1}, n_{h_2}, l_{h_2}; L_h, J_h; F_h, F_{hz}\rangle_h. \quad (\text{A2})
\end{aligned}$$

The electron (hole) pair states in Eq. (A2) are defined in the same way as the exciton basis states Eq. (A1):

$$\begin{aligned}
|n_{e_1}, l_{e_2}, n_{e_1}, l_{e_2}; L_e, S; F_e, F_{ez}\rangle_e & = \sum \langle L_e, S; M_e, S_z | F_e, F_{ez} \rangle \langle l_{e_1}, l_{e_2}; m_{e_1}, m_{e_2} | L_e, M_e \rangle \\
& \quad \times \langle \frac{1}{2}, \frac{1}{2}; s_{z_1}, s_{z_2} | S, S_z \rangle |n_{e_1}, l_{e_1}, m_{e_1}; \frac{1}{2}, s_1\rangle |n_{e_2}, l_{e_2}, m_{e_2}; \frac{1}{2}, s_2\rangle
\end{aligned}$$

and

$$\begin{aligned}
|n_{h_1}, l_{h_2}, n_{h_1}, l_{h_2}; L_h, J; F_h, F_{hz}\rangle_h & = \sum \langle L_h, J; M_h, J_z | F_h, F_{hz} \rangle \langle l_{h_1}, l_{h_2}; m_{h_1}, m_{h_2} | L_h, M_h \rangle \\
& \quad \times \langle \frac{3}{2}, \frac{3}{2}; j_{z_1}, j_{z_2} | J, J_z \rangle |n_{h_1}, l_{h_1}, m_{h_1}; \frac{3}{2}, j_1\rangle |n_{h_2}, l_{h_2}, m_{h_2}; \frac{3}{2}, j_2\rangle.
\end{aligned}$$

In the linear space spanned by the basis functions (A1) and (A2), both the matrix elements of the Luttinger Hamiltonian and the Coulomb interaction can be computed numerically. For simplicity, we assume an infinitely deep quantum confinement potential in our calculations; however, this method can easily be extended to deal with a finite confinement potential. The matrix elements of the Coulomb interaction in the linear space spanned by the exciton basis states, defined by Eq. (A1), and biexciton basis states, defined by Eq. (A2), can be computed numerically using a straightforward generalization of the method discussed in Ref. 7. The matrix elements of the Hamiltonian (5) are calculated using the Wigner-Eckart theorem,

$$\langle jm | T_q^{(k)} | j' m' \rangle = \frac{1}{\sqrt{2j+1}} \langle j', k; -m, q | j, -m \rangle \langle j || T^{(k)} || j' \rangle,$$

where  $T_q^{(k)}$  is a spherical tensor operator of rank  $k$ , and  $\langle j || T^{(k)} || j' \rangle$  are the so-called reduced matrix elements. The reduced matrix elements of the momentum operator  $P$  and the angular momentum  $J = \frac{3}{2}$  are given explicitly in Ref. 11.

The exciton states of interest for the analysis in the present paper are the dipole-allowed states with angular momentum  $F_x = 1$ . We construct the linear basis states for exciton and biexciton states using the same single-particle orbital wave functions used in Ref. 7. In the two-band calculation, where only  $L=0$  exciton states are dipole allowed, we used 64 basis states to obtain reasonable numerical accuracy.

In the present calculations, the exciton states with  $L=2$  are coupled directly to the exciton states with  $L=0$  as a consequence of the valence-band mixing, which induces the coupling of  $s$  and  $d$  excitons. To have  $F_x = 1$ , we need the one-pair states that have the angular momenta  $(L, J) = (0, 1)$ ,  $(2, 1)$ , and  $(2, 2)$ . Using Eq. (A1), we obtain 344 basis states.

There are two groups of biexciton states which are of special interest in optical transitions:  $F=0$  and 2. These states can be directly created in a dipole-allowed transition from the dipole allowed one-pair states (with  $F=1$ ). To obtain the same numerical accuracy as in the exciton calculation also in the biexciton state calculation, the number of

biexciton basis states constructed using Eq. (A2) is of the order of  $10^5$ , which makes a straightforward complete numerical calculation impossible. Therefore we used an evaluation procedure where we selectively choose those basis states that are directly coupled to the lowest basis state through the Coulomb interaction. Since we only need to calculate the biexciton states with  $F=0$  we can restrict the analysis to 1556 biexciton basis states.

The biexciton binding energy in QD's has been the subject of experimental and theoretical studies in recent years.<sup>6,7,17</sup> The biexciton binding energy is defined as

$$\Delta E_{xx} = 2\epsilon_x^0 - \epsilon_{xx}^0,$$

where  $\epsilon_x^0$  and  $\epsilon_{xx}^0$  are the ground-state energies of the exciton and biexciton, respectively. Using the numerical matrix diagonalization method,  $\Delta E_{xx}$  has been calculated within the parabolic-band approximation.<sup>7</sup> Here, we calculate the biexciton binding energy in the presence of the valence-band-mixing effect. To simplify the subsequent discussion, we define the exciton Rydberg energy and Bohr radius as

$$E_R = \frac{\mu_r e^4}{2\epsilon_2^2}, \quad a_B = \frac{\epsilon_2}{e^2 \mu_r},$$

respectively, where the reduced mass  $\mu_r$  is

$$\mu_r = \frac{m_e m_h}{m_e + m_h}, \quad m_h = \frac{m_0}{\gamma_1}.$$

It should be pointed out here that the exciton units used in this paper are not necessarily identical to the bulk exciton parameters. This is because the effective hole mass defined in this paper is neither the heavy-hole nor the light-hole mass in the corresponding bulk sample.

We plot the computed biexciton binding energy  $\Delta E_{xx}$  as a function of the dot radius  $R$  in Fig. 9. For these results we choose the mass ratio  $m_e/m_h = 0.5$  and the dielectric constant ratio  $\epsilon_2/\epsilon_1 = 1$ . The three curves in Fig. 9, from top to bottom, correspond to different valence-band-mixing parameters  $\mu = 0.9, 0.75$ , and  $0.5$ . The increasing biexciton binding energy with increasing  $\mu$  can be understood as follows. With  $\mu$

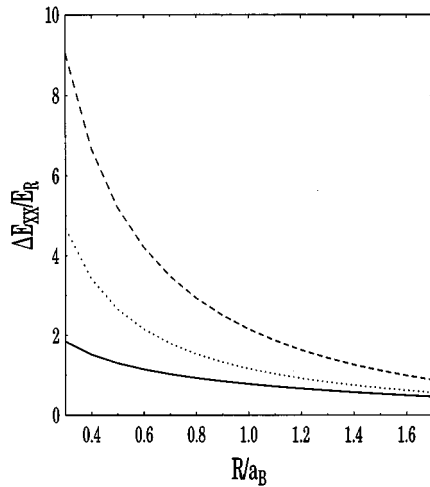


FIG. 9. Computed biexciton binding energy  $\Delta E_{xx}$  as a function of dot size  $R$ .  $m_e/m_h=0.5$ ,  $\epsilon_2/\epsilon_1=1$ ,  $\mu=0.6$  (solid),  $\mu=0.75$  (dotted), and  $\mu=0.9$  (dashed).

increasing, the heavy-hole mass increases and within the parabolic-band approximation we have shown that  $\Delta E_{xx}$  increases as  $m_e/m_h$  decreases when other parameters are unchanged.<sup>7</sup> For the dot radii of interest, the numerical calculation shows that  $\Delta E_{xx}$  is always positive.

Within the parabolic-band approximation, it can be proven that the biexciton binding energy in a dot with vanishing radius is strictly positive.<sup>6</sup> However, in the presence of the valence-band-mixing effect, the unperturbed hole wave function is no longer the same as the unperturbed electron wave function. As a result, the first-order Coulomb correc-

tion to the binding energy is not exactly canceled as in the parabolic-band approximation. Therefore the theoretical possibility exists that the binding energy becomes negative when the radius is sufficiently small.

In the present calculation we could not find negative biexciton binding energies even for the smallest dots. We cannot completely rule out that this result is caused by the accuracy limitations of our numerical procedure. As mentioned above, when we calculate the biexciton states, only the basis states which are directly coupled to the lowest basis states are taken into account. For example, we choose the state  $|1s,1s,1s,1d\rangle$  as one of the two-pair basis states, which in turn is coupled to the basis state  $|2s,1s,1s,1d\rangle$  through the Coulomb interaction. The second basis state,  $|2s,1s,1s,1d\rangle$ , is coupled with the state  $|2s,1s,1d,1d\rangle$ , through the  $s$ - $d$  wave-function mixing. However, the basis state,  $|2s,1s,1d,1d\rangle$  is not included in our calculation. Neglecting the states like  $|2s,1s,1d,1d\rangle$  has no influence on the ground-state energy without either the Coulomb interaction or valence-band mixing. However, if both interactions are included, the basis states such as  $|2s,1s,1d,1d\rangle$  contribute to the higher-order energy corrections. They become important only when the dot radius is so small that the higher-order corrections of the biexciton binding energy, which is the difference of two large numbers,  $\epsilon_{xx}$  and  $\epsilon_x$ , become important.

To verify this argument, we estimate the dot radius at which the biexciton binding energy becomes negative using perturbative analysis.<sup>6</sup> Using the material parameters given in this paper, we find that the biexciton binding energy is positive if  $R > 0.05a_B$ . Thus we conclude that for all realistic dot sizes outside the molecular regime the biexciton binding energy is always positive even in the presence of the valence-band-mixing effect.

<sup>1</sup>See, e.g., W. W. Chow, S. W. Koch, and M. Sargent III, *Semiconductor Laser Physics* (Springer-Verlag, New York, 1994).

<sup>2</sup>S. W. Koch, H. Haug, G. Schmieder, W. Bohnert, and C. Klingshirn, *Phys. Status Solidi* **89**, 431 (1978).

<sup>3</sup>C. Klingshirn and H. Haug, *Phys. Rep.* **70**, 315 (1981).

<sup>4</sup>J. Ding, H. Jeon, T. Ishihara, M. Hagerott, A. V. Nurmikko, H. Luo, N. Samarth, and J. Furdyna, *Phys. Rev. Lett.* **69**, 1707 (1992); J. Ding, H. Jeon, T. Ishihara, M. Hagerott, and A. V. Nurmikko, *Phys. Rev. B* **47**, 10 528 (1993).

<sup>5</sup>For a recent review, see L. Bányai and S. W. Koch, *Semiconductor Quantum Dots*, World Scientific Series on Atomic, Molecular and Optical Physics Vol. 2 (World Scientific, Singapore, 1993), and references therein.

<sup>6</sup>L. Bányai, *Phys. Rev. B* **39**, 8022 (1989).

<sup>7</sup>Y. Z. Hu, S. W. Koch, M. Lindberg, N. Peyghambarian, R. Pollock, and F. F. Abraham, *Phys. Rev. Lett.* **64**, 1805 (1990); Y. Z. Hu, M. Lindberg, and S. W. Koch, *Phys. Rev. B* **42**, 1713 (1990).

<sup>8</sup>H. Gießen, U. Woggon, B. Fluegel, G. Mohs, Y. Z. Hu, S. W.

Koch, and N. Peyghambarian (unpublished).

<sup>9</sup>J. M. Luttinger, *Phys. Rev.* **102**, 1030 (1956).

<sup>10</sup>L. E. Brus, *J. Chem. Phys.* **80**, 4403 (1994).

<sup>11</sup>A. Baldereschi and N. O. Lipari, *Phys. Rev. B* **8**, 2697 (1973).

<sup>12</sup>J. B. Xia, *Phys. Rev. B* **40**, 8500 (1989).

<sup>13</sup>P. C. Sercel and K. J. Vahala, *Phys. Rev. B* **42**, 3690 (1990).

<sup>14</sup>A. I. Ekimov, F. Hache, M. C. Schanne-Klein, D. Ricard, C. Flytzanis, I. A. Kudryavtsev, T. V. Yazeva, A. Rodina, and Al. L. Efros, *J. Opt. Soc. Am. B* **10**, 100 (1993).

<sup>15</sup>K. Meissner, B. Fluegel, H. Gießen, G. Mohs, R. Binder, A. Paul, S. W. Koch, and N. Peyghambarian, *Phys. Rev. B* **50**, 17 647 (1994).

<sup>16</sup>E. U. Condon and S. H. Shortly, *The Theory of Atomic Spectra* (Cambridge University Press, New York, 1951).

<sup>17</sup>V. Klimov, S. Hunsche, and H. Kurz, *Phys. Rev. B* **50**, 8110 (1994); Y. Masumoto, S. Okamoto, and S. Katayanagi, *ibid.* **50**, 18 658 (1994); K. I. Kang, A. D. Kepner, S. V. Gaponenko, S. W. Koch, Y. Z. Hu, and N. Peyghambarian, *ibid.* **48**, 15 449 (1993).